

# RankByGene: Gene-Guided Histopathology Representation Learning Through Cross-Modal Ranking Consistency

Wentao Huang<sup>1\*</sup> Meilong Xu<sup>1</sup> Xiaoling Hu<sup>2</sup> Shahira Abousamra<sup>3</sup> Aniruddha Ganguly<sup>1</sup>  
 Saarthak Kapse<sup>1</sup> Alisa Yurovsky<sup>1</sup> Prateek Prasanna<sup>1</sup> Tahsin Kurc<sup>1</sup>  
 Joel Saltz<sup>1</sup> Michael L. Miller<sup>4</sup> Chao Chen<sup>1</sup>

<sup>1</sup>Stony Brook University, NY, USA

<sup>2</sup>Athinoula A. Martinos Center for Biomedical Imaging,  
 Massachusetts General Hospital and Harvard Medical School, MA, USA

<sup>3</sup>Department of Biomedical Data Science, Stanford University, CA, USA

<sup>4</sup>Department of Pathology and Cell Biology, Columbia University, NY, USA

## Abstract

*Spatial transcriptomics (ST) provides essential spatial context by mapping gene expression within tissue, enabling detailed study of cellular heterogeneity and tissue organization. However, aligning ST data with histology images poses challenges due to inherent spatial distortions and modality-specific variations. Existing methods largely rely on direct alignment, which often fails to capture complex cross-modal relationships. To address these limitations, we propose a novel framework that aligns gene and image features using a ranking-based alignment loss, preserving relative similarity across modalities and enabling robust multi-scale alignment. To further enhance the alignment’s stability, we employ self-supervised knowledge distillation with a teacher-student network architecture, effectively mitigating disruptions from high dimensionality, sparsity, and noise in gene expression data. Extensive experiments on gene expression prediction and survival analysis demonstrate our framework’s effectiveness, showing improved alignment and predictive performance over existing methods and establishing a robust tool for gene-guided image representation learning in digital pathology.*

## 1. Introduction

Digital pathology has advanced significantly in recent years, thanks to the availability of large number of digitized slides and rapid development of deep learning. Powerful learning methods have been proposed for image-based prediction at different scales, including individual cells [5, 22, 25], larger structures like glands [29, 69, 75], regions

of interest [20, 33], and the whole slide [13, 28, 32, 34, 42]. However, these methods, despite their promise, are fundamentally limited by the amount of information one can extract from a digital slide. Most clinical outcomes are given at a whole slide-level. Due to the heterogeneity of the tissue microenvironment, it is very difficult for a machine learning algorithm to directly connect localized cell morphology and spatial context with clinical outcomes. Connecting cell morphology/context with their actual functionality is the missing link and can be the key to advancing image-based diagnosis and prognosis.

Transcriptomics [49, 72] reflects the genome-wide quantification of gene expression within a tissue, and these approaches provide a snapshot of gene activity within a variably heterogeneous collection of cells. Single-cell RNA sequencing [62, 63] attempts to address this cellular heterogeneity by profiling gene expression within individual level, enabling more precise cell typing and characterization. Despite its high resolution, this approach disrupts tissue architecture and loses the critical spatial context that defines an organized tissue [58].

Spatial transcriptomics (ST) bridges the gap by enabling gene expression profiling within tissue structures, preserving the spatial context of cellular activity [56]. It measures gene expression at specific locations, allowing for the mapping of cellular states and molecular interactions in their native micro-environments [45, 61]. This spatial dimension is crucial for studying the interactions between cells and their microenvironment, which are central to understanding disease dynamics and therapeutic responses [19, 48]. For example, ST can uncover molecular signatures unique to specific tumor regions, such as the core, invasive margins, and immune-infiltrated zones, enabling a nuanced view of tumor heterogeneity [31].

\*Email: wenthuang@cs.stonybrook.edu.

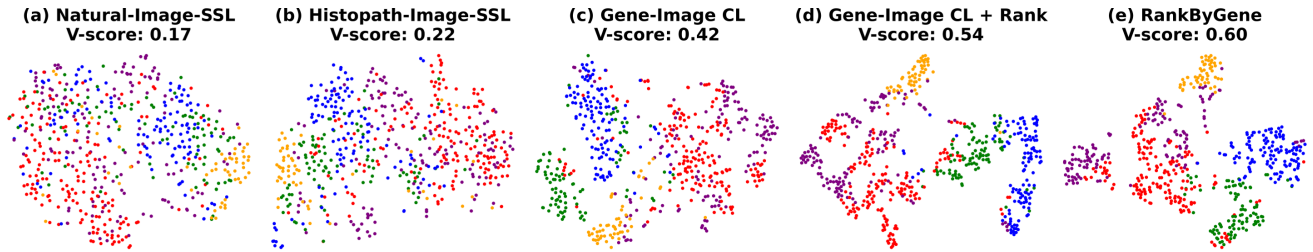


Figure 1. t-SNE visualization [66] of image representation from different methods. (a) Natural-Image-SSL. (b) Histopath-Image-SSL. (c) Gene-Image CL (d) Gene-Image CL with ranking loss. (e) RankByGene. We first use K-means clustering to assign a class label to each spot based on gene expression values. Then, we apply t-SNE to visualize the image features corresponding to each spot and color them according to their assigned class labels. A higher v-score [57] indicates that the image representation more precisely captures the distribution of gene expression values. Adding ranking loss (d) enhances the separability between image features of different classes. Our method (e), with both ranking loss and distillation shows the highest separability.

ST data provides new opportunities to enhance existing image-based prediction methods with novel biological information. Most ST data have both localized gene expressions and their corresponding histology image patches. One can exploit the two complementary modalities at a fine scale, unveiling the subtle visual cues from cell morphology and context that capture cell functionality. In this paper, we study the problem of learning gene-guided image representations through ST data. In particular, we use the gene expression to better align image features, so that these image features encode cell-functionality-specific visual information. As we will demonstrate in experiments, these gene-guided image features will improve image-based prediction of clinical outcomes. The learned features can be applied broadly to any image-only cohort, benefiting the digital pathology community.

Despite its scientific potential, multi-modal representation learning with ST data is challenging for various reasons. First and most importantly, it is fundamentally unknown how well the image and gene expressions could align. Different modalities may contain different information; ensuring complete alignment can be difficult or even impossible [27]. Secondly, the image and gene features are encoded with different networks and have different initial representation powers; while images can be encoded with CNNs and can be initialized with powerful foundational models [14, 15, 68, 70, 71, 74], typically gene feature encoding can only be based on fully-connected networks and trained from scratch [30, 46, 73]. Furthermore, the gene expression data is extremely high-dimensional (with more than 15,000 genes per sample) and very sparse (on average, 80% of gene expression values are zeros [30]). Finally, as a novel technology, available ST data often suffers from experimental artifacts, such as spatial dependent noise [6] and sparsity [35, 36].

To address these challenges, methods have been proposed to map both image patches and gene expressions into

a shared latent feature space. Self-supervised contrastive learning losses have been adopted to ensure the image features and gene features from the same location (called a *spot*) are mapped together [30]. The standard contrastive loss, however, overlooks the potential similarity between different spots. Xie et al. [73] employ a smoothed variant of the CLIP loss [55] to encourage spots with similar image patches or similar gene expressions to be mapped closer in the feature space. These methods, however, do not fully address the aforementioned challenges and lack an effective global strategy to align multi-modal features.

In this paper, we propose a novel approach to align image and gene features across multiple scales, both locally and globally. The alignment method is designed to be robust to modality-specific distortions, addressing the challenges outlined earlier. Specifically, we introduce an innovative ranking-based alignment loss that captures the relative similarity ordering of feature representations across modalities. By enforcing consistency in cross-modal ranking, we ensure that the similarity relationships between gene expression features are reflected in the corresponding image features. This ranking-based approach offers several key advantages. First, it facilitates alignment across both local and global scales, enabling even distant features to interact and align. This global alignment complements the existing local matching of image and gene features of the same spot [46, 73]. Second, by focusing on matching rankings rather than exact similarity values, our method is more robust to distortions, allowing it to tolerate similarity variations especially between features that are far apart from one another.

To further enhance the robustness of the alignment process, we adopt a self-supervised knowledge distillation approach to stabilize the learning of gene-informed image representations. By utilizing a teacher-student network architecture with both weakly and strongly augmented image patches, we ensure that the student network effectively

learns the aligned features. This approach helps the student network remain resilient to potential disruptions arising from imperfections in the gene expressions, such as high dimensionality, sparsity, and noisy or missing values.

Figure 1 shows the t-SNE visualization [66] of image features obtained from various methods: natural image-only self-supervised learning (SSL), histopathology image-only SSL, gene-image contrastive learning (CL), gene-image CL with ranking loss, and our method. Compared to other methods, the image features generated by our approach effectively capture the distribution of gene expression values.

In summary, we propose a novel multi-modal feature alignment method that integrates pathology images and ST data, enabling robust gene-informed image representation learning. Our contributions are three-fold:

- We introduce a new cross-modal ranking consistency mechanism to enhance multi-modal alignment, achieving alignment at both local and global scales while remaining robust to distortions over long-range distances.
- We apply a knowledge distillation approach to the multi-modal alignment task, further improving the robustness of the alignment process despite imperfections in gene expression features.
- Extensive experiments across multiple downstream tasks, including gene expression prediction and survival prediction, demonstrate the superior performance of our framework compared to existing self-supervised alignment methods.

## 2. Related Work

**Histopathology Image Analysis.** Histopathology image analysis is regarded as the gold standard for cancer diagnosis and treatment [9, 41, 50]. Due to the huge resolution of whole slide images (WSIs) and the difficulty of obtaining patch-level labels, WSI analysis is commonly performed in a weakly supervised setting [18], where only slide-level labels are available. Typical WSI analysis tasks include classification [28, 34, 54, 59, 64, 77, 78], which predicts the presence or absence of a tumor or identifies specific tumor subtypes, and survival prediction [13, 60, 76, 79, 81], which estimates patient mortality risk. Many multiple instance learning (MIL) [28, 34, 39, 53, 77, 82] based frameworks have been proposed to model relationships between patches more effectively, enabling more accurate slide-level predictions.

**Image Feature Learning in Histopathology.** The performance of WSI analysis heavily relies on image feature learning. With advancements in self-supervised learning (SSL) in computer vision, methods like SimCLR [16], MoCo [24], and DINO [11] have been adapted for image feature learning in histopathology, leading to the development of various foundation models pretrained on WSI, such

as CTransPath [70], HIPT [14], and more recent models like UNI [15], GigaPath [74], CHIEF [71], and Virchow [68]. These foundation models have significantly improved WSI analysis performance. Additionally, task-specific fine-tuning [37, 40, 65] techniques have been introduced to further optimize image feature learning for downstream tasks.

**Multi-Modal Pretraining in Histopathology.** With the growing availability of multi-modal data and advancements in pretraining techniques across multiple modalities, CLIP-based [8, 21, 38, 55, 80] vision-language pretraining methods have been applied to text-image pathology datasets, resulting in the development of approaches like MI-zero [43], PLIP [26], and Conch [44].

Furthermore, the recent availability of ST data [12, 30] has expanded opportunities for multimodal learning in histopathology. More challenging tasks, such as gene expression prediction [12, 17, 30], have been introduced to evaluate the robustness of pretrained image encoders. In addition, several methods for image-gene pretraining, such as BLEEP [73] and mclSTExp [46], have also been proposed to enhance image feature learning. However, these approaches may not fully capture relationships between spots, nor adequately address the noise and sparsity in gene expression data. In this work, we focus on developing a robust multi-modal alignment approach that integrates image and gene features across multiple scales to achieve more effective gene-informed image representations.

## 3. Methods

Our learning pipeline is illustrated in Figure 2. The training data consists of pairs of image patches and gene expression profiles, with each pair corresponding to a specific tissue spot. Image patches are fed into image encoders, which include both a teacher and a student encoder to facilitate knowledge distillation for gene-guided image feature learning. This setup helps stabilize the image feature learning process during alignment with gene features. Meanwhile, gene expression data is processed by a gene encoder.

Both image and gene features are mapped into a shared latent feature space. To align these features, we employ a contrastive learning loss that ensures the image and gene features of the same tissue spot are closely matched. Additionally, we introduce a cross-modal ranking consistency loss to maintain the same relative ranking of similarity across spots, ensuring that for any given spot, its similarity to other spots is consistent in both image and gene feature spaces.

At inference time, we will only use the teacher image encoder to extract gene-guided image features from histopathology image patches. The feature can be used for different downstream tasks that make predictions based on histopathology images. We will first introduce the contrastive learning loss we use for spot-wise alignment, gene-

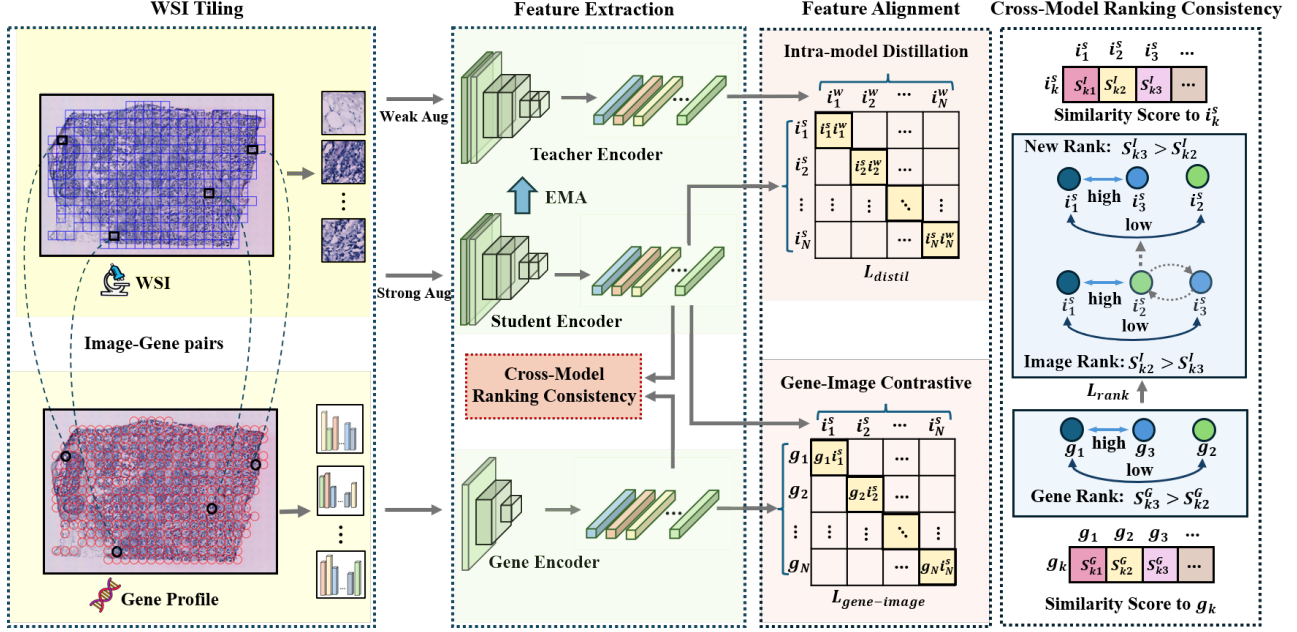


Figure 2. Overview of our *RankbyGene* framework. The framework begins with WSI Tiling, where WSIs are divided into tiles, each paired with a gene profile. In the feature extraction part, weak and strong augmentations of the image tiles are processed through a teacher encoder and student encoder, while a gene encoder extracts features from the gene profile. The feature alignment stage ensures that weakly and strongly augmented image features are aligned through intra-modal distillation loss and the image and gene features are aligned using gene-image contrastive loss. Meanwhile, our proposed cross-modal ranking consistency loss maintains consistent similarity ranking orders across two modalities.

image contrastive (Section 3.1). Next, we introduce the cross-modal ranking consistency loss (Section 3.2). We conclude this section with details on the intra-modal distillation for gene-guided image features (Section 3.3).

**Preliminaries.** Given a set of  $N$  spots,  $\{1, \dots, N\}$ , each with a pair of image patch and gene profile, we send them into two separate encoders (image encoder and gene encoder), mapping them into image features and gene features.  $I = \{i_1, i_2, i_3, \dots, i_N\}$  denotes the image features of the  $N$  spots, and  $G = \{g_1, g_2, g_3, \dots, g_N\}$  their corresponding gene features.

### 3.1. Gene-Image Contrastive Loss

To align image and gene features, we first employ the InfoNCE Loss [51], a commonly used loss function for aligning two modalities. InfoNCE encourages the model to pull positive pairs (image and gene features from the same spot) closer in the shared latent space while pushing apart negative pairs (image and gene features from different spots). The Gene-Image Contrastive loss is defined as follows:

$$\mathcal{L}_{\text{gene-image}} = - \sum_{p=1}^N \left[ \log \frac{\exp(\text{sim}(i_p, g_p)/\tau)}{\sum_{q=1}^N \exp(\text{sim}(i_p, g_q)/\tau)} \right] \quad (1)$$

where  $\text{sim}(i_*, g_*)$  is the cosine similarity between the image feature  $i_*$  and the gene feature  $g_*$ .  $\tau$  is a temperature parameter. This loss penalizes unmatched pairs by reducing their similarity while increasing the similarity between matched gene-image pairs.

### 3.2. Cross-Modal Ranking Consistency Loss

The InfoNCE loss ensures local alignment between image and gene features from the same tissue spot, but it does not address global alignment, which is essential for achieving more accurate and consistent cross-modal correspondences. Directly aligning distances between features from distant tissue spots is not practical, as long-range feature relationships may not be reliable. Instead, we propose that the relative ranking of distances between features is more robust and can provide a more trustworthy basis for alignment.

To leverage this idea, we introduce the Cross-Modal Ranking Consistency Loss. This loss function encourages the model to learn image representations while maintaining the relative similarity ordering of gene features across tissue spots. By focusing on the ranking of distances rather than exact alignments, the ranking loss facilitates a more reliable and robust global alignment. It complements the local alignment achieved by InfoNCE, while also capturing long-range interactions between features from different



tissue spots. In doing so, the ranking consistency loss promotes a more comprehensive and stable cross-modal alignment, improving both local and global correspondences.

Our ranking loss is illustrated in Figure 3. For a spot of interest,  $p$ , we want to ensure the similarity between  $p$  and two other spots,  $q$  and  $r$ , are ranked consistently in both image feature and gene feature. For simplicity, we denote by  $S_{p,q}^I = \text{sim}(i_p, i_q)$  and  $S_{p,q}^G = \text{sim}(g_p, g_q)$  the similarity between  $p$  and  $q$ 's image features and gene features. We also denote by  $S_{p,r}^I$  and  $S_{p,r}^G$  the image and gene feature similarity between  $p$  and  $r$ . Assume  $S_{p,q}^G > S_{p,r}^G$ . In other words,  $g_q$  is closer to  $g_p$  compared with  $g_r$ . We would like to ensure the image features  $i_q$  and  $i_r$  also maintain the same order. Classic ordinal ranking loss [10] will just require the image feature similarity difference  $S_{p,q}^I - S_{p,r}^I$  to be bigger than a fixed positive value  $\epsilon$ . However, this may be undesirable especially for long interactions. To better preserve the relative positions between features, we require the difference  $S_{p,q}^I - S_{p,r}^I$  to be bigger than  $S_{p,q}^G - S_{p,r}^G$ . Formally, we define the function

$$\ell(p, q, r) = (S_{p,q}^G - S_{p,r}^G) - (S_{p,q}^I - S_{p,r}^I) \quad (2)$$

and intend to enforce  $\ell(p, q, r)$  to be non-positive for all triplets  $(p, q, r)$ . Figure 3 illustrates different cases. In practice, we rewrite the function with the sign function

$$\ell(p, q, r) = \text{sign}(S_{p,q}^G - S_{p,r}^G) \cdot [(S_{p,q}^G - S_{p,r}^G) - (S_{p,q}^I - S_{p,r}^I)] \quad (3)$$

This way, even if  $S_{p,q}^G < S_{p,r}^G$ , requiring  $\ell(\cdot)$  to be non-positive will still enforce the relative ranking consistency between image and gene features of the three spots.

Finally, we need a loss to enforce  $\ell(\cdot)$  to be nonnegative. To this end, we use a variant of the classic hinge loss,  $\max\{0, \ell(p, q, r)\}$ , which incurs penalty if and only if  $\ell(p, q, r)$  is positive. Enumerating through all triplets, we have the cross-modal ranking consistency loss

$$\mathcal{L}_{\text{rank}} = \sum_p \sum_{q \neq p} \sum_{r \neq p, q} \max\{0, \ell(p, q, r)\} \quad (4)$$

**Accelerating the Computation.** During training, at each iteration, we will apply the loss to all spots within a mini-batch.  $N$  becomes the batch size. However, this can still be computationally expensive, as it compares  $O(N^3)$  pairs of spots. To alleviate the burden, we still enumerate through all  $p$ 's. But for each  $p$ , instead of enumerating through all  $O(N^2)$   $(q, r)$  pairs, we only sample  $O(N)$  random  $(q, r)$  pairs. In particular, taking the list of spots except  $p$ ,  $L = (1, \dots, p-1, p+1, \dots, N)$ . We randomly shuffle the sequence, getting a shuffled list,  $L'$ . We go through the list,  $L'$ , each time taking two consecutive spots as  $q$  and  $r$ . For the last spot, we will pair it with the first spot in  $L'$ . This

gives us  $N - 1$  sample  $(q, r)$  pairs, and ensures each spot appears in two of the sampled pairs. This reasonably covers similarity rankings of all the spots, but only using  $O(N^2)$  triplets.

### 3.3. Intra-Modal Distillation Loss

In our framework, we employ a teacher-student network architecture to achieve robust feature representations across differently augmented instances of the same pathology image, drawing on recent advances in self-supervised knowledge distillation for single-modality representation learning [11, 52]. To enhance stability and invariance in feature embeddings produced by the patch encoder, we apply both weak and strong augmentations to simulate the typical variability found in pathology images.

In this setup, the weakly augmented image is processed through the teacher encoder, while the strongly augmented version passes through the student encoder. The weights of the teacher encoder are incrementally updated using an Exponential Moving Average (EMA) of the student encoder's weights, which helps stabilize the training. This strategy ensures that the student gradually learns stable features over time.

To enforce the consistency between the representations of the two augmented versions, we introduce the Image Consistency Loss:

$$\mathcal{L}_{\text{distil}} = -\frac{1}{N} \sum_{p=1}^N \left[ \log \frac{\exp(\text{sim}(i_p^w, i_p^s)/\tau)}{\sum_{q=1}^N \exp(\text{sim}(i_p^w, i_q^s)/\tau)} \right] \quad (5)$$

where  $N$  is the batch size,  $i_p^w$  is the feature obtained from the weakly augmented image using the teacher image encoder, and  $i_p^s$  is the feature from the strongly augmented image using the student image encoder. Minimizing this loss encourages the image encoder to learn representations resilient to such variations and potential disruptions from gene expression data characteristics, such as high dimensionality, sparsity, noise, and missing values.

### 3.4. Overall Loss Function

The total loss is a weighted sum of the Gene-Image Contrastive Loss, the Cross-Modal Ranking Loss, and the Intra-Modal Distillation Loss:

$$\mathcal{L}_{\text{total}} = \mathcal{L}_{\text{gene-image}} + \lambda_1 \mathcal{L}_{\text{rank}} + \lambda_2 \mathcal{L}_{\text{distil}} \quad (6)$$

where  $\lambda_1$  and  $\lambda_2$  are hyperparameters that control the balance between the ranking consistency loss and the distillation loss, respectively.

## 4. Experiments and Results

### 4.1. Dataset

In this study, we use the breast and lung ST data from the HEST-1k dataset [30], which collects publicly avail-

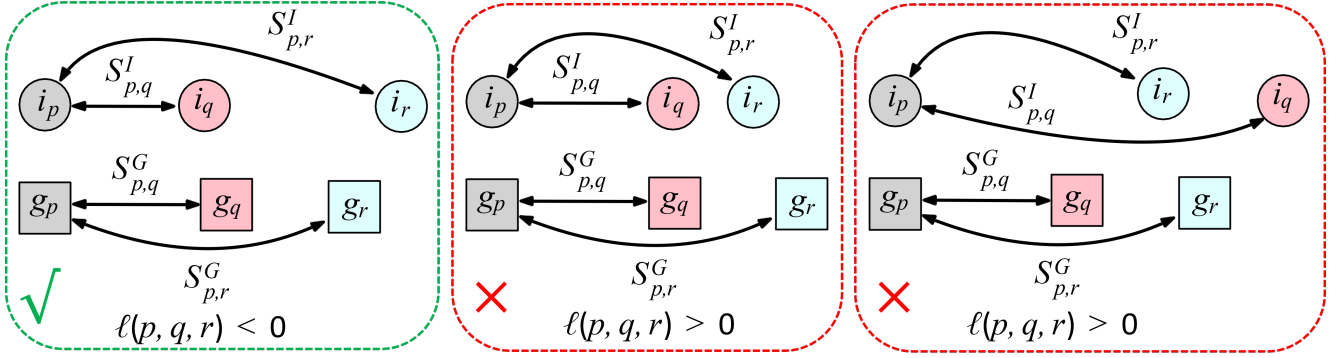


Figure 3. Illustration of the ranking loss intuition, when the gene features  $g_q$  is closer to  $g_p$  than  $g_r$ . Note the similarity is inverse proportional to the distance. **Left:**  $i_q$  is also closer to  $i_p$  than  $i_r$ , and furthermore, the gap between image feature similarities  $S_{p,q}^I$  and  $S_{p,r}^I$  is bigger than the gap between gene feature similarities  $S_{p,q}^G$  and  $S_{p,r}^G$ . This is the desirable case where  $\ell(p, q, r)$  is negative. **Middle:** when the similarity ranking is the same between gene and image features, but when the gap between image feature similarities is smaller than the gap between gene feature similarities.  $\ell(p, q, r)$  is positive, and will incur penalty. **Right:** when the similarity order is inconsistent,  $\ell(p, q, r)$  is positive. Undesirable.

able, high-quality ST datasets and applies standardized processing to all collected data. For WSIs, we utilize the TCGA-BRCA (Breast Invasive Carcinoma) and TCGA-LUAD (Lung Adenocarcinoma) datasets from TCGA cohorts [1]. Detailed descriptions of each dataset will be provided in the following sections.

**Breast ST datasets.** The Breast ST dataset used for training [7] contains 36 ST samples. Each sample contains approximately 15,000 genes, and after preprocessing, we obtained 13,620 spots from all ST samples. Following the external evaluation approach described in [17], we selected two Visium breast ST samples from 10x Genomics to evaluate our model’s performance in predicting gene expression. The first sample is the Human Breast Cancer: Visium Fresh Frozen, Whole Transcriptome [3], containing 4,898 spots. The second sample is the Human Breast Cancer (Block A Section 1) Visium [2], containing 3,813 spots. We refer to the first sample [3] as Breast-ST1 and the second sample [2] as Breast-ST2.

**Lung ST datasets.** The Lung ST dataset used for training originates from [47] and consists of 6 ST samples, each containing approximately 18,000 genes, with a total of 12,891 spots. For testing, we select 4 lung ST samples from [67], which we refer to as Lung-ST, containing a total of 1,831 spots.

**Cancer-Specific Gene List Selection** To manage the high dimensionality of gene expression data, existing methods typically select a list of highly expressed genes for gene-image alignment, such as choosing the top 250 [17], top 100 [12], or top 50 [17, 30, 73] genes. However, this approach may overlook low-expression but significant genes, which can be crucial for downstream WSI analysis tasks. To help the model align images with cancer-specific genes, we se-

lect prognosis-related genes from the Human Protein Atlas [4]. Specifically, we first selected genes related to breast and lung cancer and then intersected these with genes in the ST data, resulting in final gene lists of 447 genes for breast ST and 1916 genes for lung ST data. We utilized these gene lists to train both our model and all multi-modal baseline methods. We will provide more details about the gene lists in the supplementary materials.

**WSI Datasets.** We use survival prediction on TCGA-BRCA (1,022 WSIs) and TCGA-LUAD (515 WSIs) as our downstream task. Following the preprocessing steps in [42], we cut patches at  $224 \times 224$  pixels with  $20\times$  magnification.

## 4.2. Evaluation Metrics

For the gene expression prediction task, following previous methods [17, 30, 73], we use Mean Squared Error (MSE), Mean Absolute Error (MAE), and Pearson Correlation Coefficient (PCC) as evaluation metrics to evaluate. For the survival prediction task, we adopt a 5-fold cross-validation setting as in [13, 76, 81] and use the cross-validated Concordance Index (C-Index) as the evaluation metric.

## 4.3. Implementation Details

A typical pipeline for our method consists of two stages. In the training stage, we first filter the genes using the selected cancer-related gene list, followed by multi-modal training with Breast ST [7] and Lung ST [47] dataset. In the testing stage, the trained image encoder extracts features for downstream tasks. The image encoder trained on Breast ST [7] dataset is evaluated on Breast-ST1, Breast-ST2, and TCGA-BRCA datasets, while the image encoder trained on Lung ST [47] dataset is evaluated on Lung-ST and TCGA-LUAD datasets.

Image Encoder	Breast-ST1			Breast-ST2			Lung-ST			Image Encoder	C-Index	
	MAE ↓	MSE ↓	PCC ↑	MAE ↓	MSE ↓	PCC ↑	MAE ↓	MSE ↓	PCC ↑		TCGA-BRCA	TCGA-LUAD
ResNet-50 [23]	0.3633	0.2716	0.0867	0.4042	0.2982	0.1265	0.3105	0.2043	0.0345	ResNet-50 [23]	0.5859 ± 0.0521	0.5631 ± 0.0443
CTransPath [70]	0.3572	0.2698	0.0983	0.3994	0.2957	0.1423	0.2945	0.1911	0.0395	CTransPath [70]	0.6413 ± 0.0469	0.5742 ± 0.0363
UNI [15]	0.3559	0.2648	0.1063	0.4096	0.3178	0.1398	0.2731	0.1724	0.0432	UNI [15]	0.6684 ± 0.0432	0.5865 ± 0.0254
HEST-FT [30]	0.3469	0.2552	0.1269	0.4071	0.3079	0.1592	0.2926	0.1874	0.0682	HEST-FT [30]	0.6531 ± 0.0453	0.5728 ± 0.0321
BLEEP [73]	0.3475	0.2571	0.1198	0.3982	0.2954	0.1437	0.2879	0.1806	0.0751	BLEEP [73]	0.6716 ± 0.0394	0.5778 ± 0.0383
<i>RankByGene</i>	<b>0.3412</b>	<b>0.2487</b>	<b>0.1803</b>	<b>0.3964</b>	<b>0.2927</b>	<b>0.1762</b>	<b>0.2662</b>	<b>0.1677</b>	<b>0.1019</b>	<i>RankByGene</i>	<b>0.6814 ± 0.0512</b>	<b>0.5945 ± 0.0293</b>

(a) Gene expression prediction results.

(b) Survival analysis results.

Table 1. Results for the tasks of gene expression prediction and survival analysis using different patch encoders. We use Breast-ST1, Breast-ST2, and Lung-ST datasets for gene expression prediction. The slide-level prediction is performed using the ABMIL [28] framework.

We use UNI [15] as the backbone for the image encoder, followed by a 3-layer MLP as the projection head. A 3-layer MLP is also employed for the gene encoder, consistent with the previous method [73]. Both image and gene feature dimensions are set to 1024. For the image encoder, the learning rate is set to 0.0001, while for the gene encoder, it is set to 0.001. The other training settings and test setting are detailed in the supplementary materials.

#### 4.4. Performance Comparison

We compare our method with image-only pretrained baselines, including ResNet-50 [23] (pretrained on ImageNet), CTransPath [70] and UNI [15] (both pretrained on pathology images), as well as gene-guided image feature learning baselines HEST-FT [30] and BLEEP [73].

**Gene Prediction.** As shown in Table 1a, *RankByGene* outperforms all baseline methods across the Breast-ST1, Breast-ST2, and Lung-ST datasets. Specifically, *RankByGene* achieves 11% to 42% improvement in PCC over the best baseline performance in each dataset. These results indicate that our method achieves stronger alignment between the image and gene expression data, with the obtained gene-informed image features effectively capturing the underlying global relationships between spots.

**Survival Analysis.** Using the models trained on Breast ST and Lung ST datasets, we evaluate their performance on survival prediction using TCGA-BRCA and TCGA-LUAD WSIs, respectively. Table 1b presents the performance of different methods on these two datasets. We use the image encoder from each method to extract features on patches, then apply the ABMIL [28] framework to aggregate all patch-level features for slide-level prediction. The table shows that *RankByGene* achieves the highest C-Index of 0.6814 on the TCGA-BRCA dataset and 0.5945 on the TCGA-LUAD dataset compared to all baseline methods. The strong performance on these two datasets suggests that the improved image-gene alignment enables the model to capture survival-related signals more effectively, highlighting the potential of our method to enhance performance on challenging downstream tasks.

#### 4.5. Ablation Study

**Weight of Cross-Modal Ranking Consistency Loss.** We compare the effect of different values for the weight of the ranking consistency loss  $\lambda_1$  on the Breast-ST dataset. The results in Table 2a show that the model is robust to the choice of the hyperparameter. The performance across all the tested values  $\lambda_1 > 0$  significantly outperforms the baselines, with the best result using  $\lambda_1 = 5$ .

**Weight of Intra-Modal Distillation Loss.** Table 2b presents the ablation study results for the image consistency loss weight  $\lambda_2$  on the Breast-ST1 dataset. Our method shows stable performance across MAE, MSE, and PCC at various values of  $\lambda_2$ , with consistent improvements over the baseline methods. These results indicate the benefits of incorporating image consistency loss, as it further enhances the robustness of image feature learning during alignment with gene features.

**Ablation Study on Loss Component.** Table 2c presents the ablation study results on the impact of individual loss components on the Breast-ST1 dataset. When both loss components are removed, the model exhibits the lowest PCC and higher MAE and MSE values. Including either  $\mathcal{L}_{\text{rank}}$  or  $\mathcal{L}_{\text{distil}}$  enhances performance, with the best results achieved when both components are applied. The results indicate that both the ranking loss and the image consistency loss contribute significantly to the model’s performance.

Table 2d presents the results of applying our method to different image encoders on the Breast ST1 dataset, specifically ResNet50 (a CNN-based model pretrained on ImageNet) and UNI (a ViT-based model pretrained on pathology images using the DINO framework [11]). The results demonstrate that our method consistently enhances the performance of each encoder in the gene prediction task, as evidenced by lower MAE and MSE values and higher PCC scores. This finding shows the adaptability of our approach, demonstrating its effectiveness across various encoder architectures.

$\lambda_1$	Breast-ST1			$\lambda_2$	Breast-ST1			$\mathcal{L}_{rank}$	$\mathcal{L}_{distil}$	Breast-ST1			Encoder	Breast-ST1		
	MAE ↓	MSE ↓	PCC ↑		MAE ↓	MSE ↓	PCC ↑			MAE ↓	MSE ↓	PCC ↑		MAE ↓	MSE ↓	PCC ↑
0	0.3442	0.2516	0.1542	0	0.3455	0.2535	0.1362	✗	✗	0.3469	0.2552	0.1269	ResNet50	0.3633	0.2716	0.0867
2	0.3431	0.2499	0.1776	0.5	0.3438	0.2512	0.1509	✓	✗	0.3455	0.2535	0.1362	ResNet50 + Ours	<b>0.3573</b>	<b>0.2682</b>	<b>0.1035</b>
5	<b>0.3412</b>	<b>0.2487</b>	<b>0.1803</b>	1	<b>0.3412</b>	<b>0.2487</b>	<b>0.1803</b>	✗	✓	0.3442	0.2516	0.1542	UNI	0.3559	0.2648	0.1063
10	0.3427	0.2505	0.1762	2	0.3436	0.2505	0.1544	✓	✓	<b>0.3412</b>	<b>0.2487</b>	<b>0.1803</b>	UNI + Ours	<b>0.3412</b>	<b>0.2487</b>	<b>0.1803</b>

(a) Ablation study of  $\lambda_1$ .(b) Ablation study of  $\lambda_2$ .

(c) Ablation study of loss components.

(d) Ablation study of generalizability.

Table 2. RankByGene ablation experiments. We conduct all ablation experiments on the gene expression prediction task and the Breast-ST1 dataset.

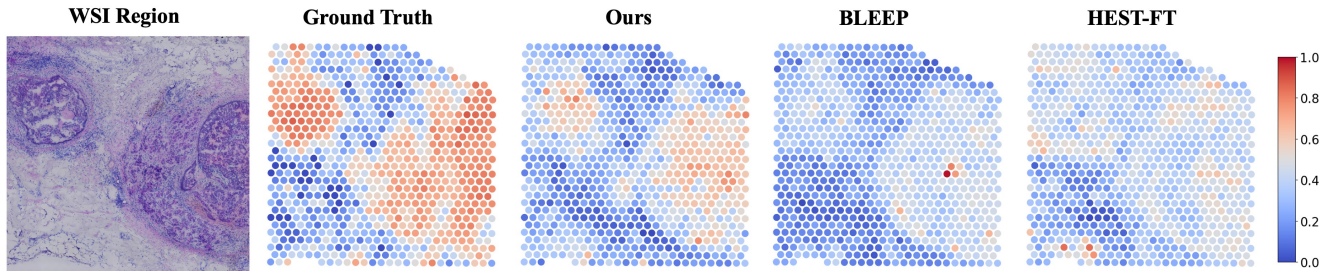


Figure 4. Visualization of PTGES3 gene expression predictions from different methods, with all values normalized to the range of 0 to 1. Compared to the baseline, our predictions show the closest match to the ground truth.

#### 4.6. Qualitative Result

**Rank Accuracy During Training.** We define Rank Accuracy as a metric to evaluate whether the ranking relationships among gene features are effectively captured by the image features during training. After the end of each epoch, Rank Accuracy is calculated as follows: the first gene-image pair in each batch is randomly selected as the anchor pair, along with two additional target pairs. Rank Accuracy is determined by checking whether the target pair with higher gene feature similarity to the anchor pair also has a higher image feature similarity. This process is repeated eight times to calculate the final Rank Accuracy. In Figure 5, we compare the change of the rank accuracy during training between different methods. The figure shows that our method achieves a larger improvement in accuracy during training compared to the baseline methods, suggesting that the rank relationships in the gene features are effectively captured by image features during the training process.

**Visualization of Cancer Marker Gene.** To evaluate the accuracy of our model’s predictions for critical genes, we selected PTGES3 as the marker gene for visualization on the Breast-ST1 dataset due to its association with poor prognosis in breast invasive carcinoma across two independent cohorts [4]. We visualized the gene prediction values for the PTGES3 from different methods across each spot, including ground truth values and the corresponding WSI region, as shown in Figure 4. Compared to the baseline method,

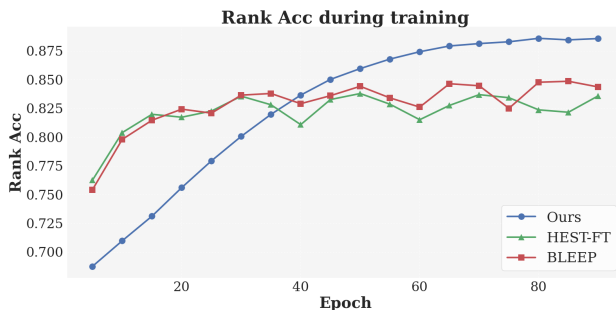


Figure 5. Rank accuracy for different methods during training.

our approach provides more accurate predictions for the PTGES3, demonstrating its effectiveness in capturing important gene expression patterns. We also provide visualizations of other marker genes for lung cancer in the supplementary materials.

#### 5. Conclusion

Our proposed framework establishes a robust and scalable approach for efficiently aligning spatial transcriptomics data with histopathology images, overcoming key challenges in cross-modal alignment. We propose a ranking-based mechanism to capture similarity relationships between gene and image features, facilitating alignment that is resilient to distortions and effective across both local and global scales. This approach preserves essential spatial and



molecular patterns, which is critical for accurately capturing the biological complexity of tissue structures. Additionally, our use of a self-supervised knowledge distillation method further enhances the alignment process, enabling the model to adaptively handle the high dimensionality, sparsity, and noise inherent in gene expression data. Through comprehensive experiments, we demonstrate our framework not only improves alignment quality but also enhances predictive capabilities in gene expression prediction and survival analysis. Ultimately, this work provides a foundational tool for multi-modal representation learning in digital pathology.

## References

- [1] The cancer genome atlas program. <https://www.cancer.gov/tcga>, 2019. 6
- [2] Human breast cancer (block a section 1). <https://www.10xgenomics.com/datasets/human-breast-cancer-block-a-section-1-1-standard-1-1-0>, 2020. 6
- [3] Human breast cancer: Visium fresh frozen, whole transcriptome. <https://www.10xgenomics.com/datasets/human-breast-cancer-visium-fresh-frozen-whole-transcriptome-1-standard>, 2022. 6
- [4] The human protein atlas. <https://www.proteinatlas.org/humanproteome/cancer>, 2024. 6, 8, 13
- [5] Shahira Abousamra, David Belinsky, John Van Arnam, Felicia Allard, Eric Yee, Rajarsi Gupta, Tahsin Kurc, Dimitris Samaras, Joel Saltz, and Chao Chen. Multi-class cell detection using spatial context representation. In *ICCV*, 2021. 1
- [6] Mohammed Abid Abrar, M Kaykobad, M Saifur Rahman, and Md Abul Hassan Samee. Novatest: identifying genes with location-dependent noise variance in spatial transcriptomics data. *Bioinformatics*, 2023. 2
- [7] Alma Andersson, Ludvig Larsson, Linnea Stenbeck, Fredrik Salmén, Anna Ehinger, Sunny Z Wu, Ghamdan Al-Eryani, Daniel Roden, Alex Swarbrick, Åke Borg, et al. Spatial deconvolution of her2-positive breast cancer delineates tumor-associated cell type interactions. *Nature communications*, 2021. 6, 13, 14, 17
- [8] Alex Andonian, Shixing Chen, and Raffay Hamid. Robust cross-modal representation learning with progressive self-distillation. In *CVPR*, 2022. 3
- [9] Laura Barisoni, Kyle J Lafata, Stephen M Hewitt, Anant Madabhushi, and Ulysses GJ Balis. Digital pathology and computational image analysis in nephropathology. *Nature Reviews Nephrology*, 2020. 3
- [10] Chris Burges, Tal Shaked, Erin Renshaw, Ari Lazier, Matt Deeds, Nicole Hamilton, and Greg Hullender. Learning to rank using gradient descent. In *ICML*, 2005. 5
- [11] Mathilde Caron, Hugo Touvron, Ishan Misra, Hervé Jégou, Julien Mairal, Piotr Bojanowski, and Armand Joulin. Emerging properties in self-supervised vision transformers. In *ICCV*, 2021. 3, 5, 7
- [12] Jiawen Chen, Muqing Zhou, Wenrong Wu, Jinwei Zhang, Yun Li, and Didong Li. Stimage-1k4m: A histopathology image-gene expression dataset for spatial transcriptomics. In *NeurIPS*, 2024. 3, 6, 15
- [13] Richard J Chen, Ming Y Lu, Wei-Hung Weng, Tiffany Y Chen, Drew FK Williamson, Trevor Manz, Maha Shady, and Faisal Mahmood. Multimodal co-attention transformer for survival prediction in gigapixel whole slide images. In *ICCV*, 2021. 1, 3, 6, 13, 14
- [14] Richard J Chen, Chengkuan Chen, Yicong Li, Tiffany Y Chen, Andrew D Trister, Rahul G Krishnan, and Faisal Mahmood. Scaling vision transformers to gigapixel images via hierarchical self-supervised learning. In *CVPR*, 2022. 2, 3
- [15] Richard J Chen, Tong Ding, Ming Y Lu, Drew FK Williamson, Guillaume Jaume, Bowen Chen, Andrew Zhang, Daniel Shao, Andrew H Song, Muhammad Shaban, et al. Towards a general-purpose foundation model for computational pathology. *Nature Medicine*, 2024. 2, 3, 7, 13
- [16] Ting Chen, Simon Kornblith, Mohammad Norouzi, and Geoffrey Hinton. A simple framework for contrastive learning of visual representations. In *ICML*, 2020. 3
- [17] Youngmin Chung, Ji Hun Ha, Kyeong Chan Im, and Joo Sang Lee. Accurate spatial gene expression prediction by integrating multi-resolution features. In *CVPR*, 2024. 3, 6, 13
- [18] Thomas G Dietterich, Richard H Lathrop, and Tomás Lozano-Pérez. Solving the multiple instance problem with axis-parallel rectangles. *Artificial intelligence*, 1997. 3
- [19] Ruiwen Ding, Prateek Prasanna, Germán Corredor, Cristian Barrera, Philipp Zens, Cheng Lu, Priya Velu, Patrick Leo, Niha Beig, Haojia Li, et al. Image analysis reveals molecularly distinct patterns of tils in nslc associated with treatment outcome. *NPJ precision oncology*, 2022. 1
- [20] Juan P Dominguez-Morales, Lourdes Duran-Lopez, Nicolò Marini, Saturnino Vicente-Diaz, Alejandro Linares-Barranco, Manfredo Atzori, and Henning Müller. A systematic comparison of deep learning methods for gleason grading and scoring. *MedIA*, 2024. 1
- [21] Shashank Goel, Hritik Bansal, Sumit Bhatia, Ryan Rossi, Vishwa Vinay, and Aditya Grover. Cyclic: Cyclic contrastive language-image pretraining. In *NeurIPS*, 2022. 3
- [22] Simon Graham, Quoc Dang Vu, Shan E Ahmed Raza, Ayesha Azam, Yee Wah Tsang, Jin Tae Kwak, and Nasir Rajpoot. Hover-net: Simultaneous segmentation and classification of nuclei in multi-tissue histology images. *MedIA*, 2019. 1
- [23] Kaiming He, Xiangyu Zhang, Shaoqing Ren, and Jian Sun. Deep residual learning for image recognition. In *CVPR*, 2016. 7, 14
- [24] Kaiming He, Haoqi Fan, Yuxin Wu, Saining Xie, and Ross Girshick. Momentum contrast for unsupervised visual representation learning. In *CVPR*, 2020. 3, 14
- [25] Fabian Hörst, Moritz Rempe, Lukas Heine, Constantin Seibold, Julius Keyl, Giulia Baldini, Selma Ugurel, Jens Siveke, Barbara Grünwald, Jan Egger, et al. Cellvit: Vision transformers for precise cell segmentation and classification. *MedIA*, 2024. 1

- [26] Zhi Huang, Federico Bianchi, Mert Yuksekgonul, Thomas J Montine, and James Zou. A visual–language foundation model for pathology image analysis using medical twitter. *Nature Medicine*, 2023. 3
- [27] Minyoung Huh, Brian Cheung, Tongzhou Wang, and Phillip Isola. Position: The platonic representation hypothesis. In *ICML*, 2024. 2
- [28] Maximilian Ilse, Jakub Tomczak, and Max Welling. Attention-based deep multiple instance learning. In *ICML*, 2018. 1, 3, 7, 15
- [29] Fabian Isensee, Paul F Jaeger, Simon AA Kohl, Jens Petersen, and Klaus H Maier-Hein. nnu-net: a self-configuring method for deep learning-based biomedical image segmentation. *Nature Methods*, 2021. 1
- [30] Guillaume Jaume, Paul Doucet, Andrew H Song, Ming Y Lu, Cristina Almagro-Pérez, Sophia J Wagner, Anurag J Vaidya, Richard J Chen, Drew FK Williamson, Ahnong Kim, et al. Hest-1k: A dataset for spatial transcriptomics and histology image analysis. In *NeurIPS*, 2024. 2, 3, 5, 6, 7, 13, 14
- [31] Andrew L Ji, Adam J Rubin, Kim Thrane, Sizun Jiang, David L Reynolds, Robin M Meyers, Margaret G Guo, Benson M George, Annelie Mollbrink, Joseph Bergensträhle, et al. Multimodal analysis of composition and spatial architecture in human squamous cell carcinoma. *Cell*, 2020. 1
- [32] Saarthak Kapse, Pushpak Pati, Srijan Das, Jingwei Zhang, Chao Chen, Maria Vakalopoulou, Joel Saltz, Dimitris Samaras, Rajarsi R Gupta, and Prateek Prasanna. Si-mil: Taming deep mil for self-interpretability in gigapixel histopathology. In *CVPR*, 2024. 1
- [33] Han Le, Rajarsi Gupta, Le Hou, Shahira Abousamra, Danielle Fassler, Luke Torre-Healy, Richard A Moffitt, Tahsin Kurc, Dimitris Samaras, Rebecca Batiste, et al. Utilizing automated breast cancer detection to identify spatial distributions of tumor-infiltrating lymphocytes in invasive breast cancer. *The American journal of pathology*, 2020. 1
- [34] Bin Li, Yin Li, and Kevin W Eliceiri. Dual-stream multiple instance learning network for whole slide image classification with self-supervised contrastive learning. In *CVPR*, 2021. 1, 3, 13
- [35] Haoyang Li, Hanmin Li, Juexiao Zhou, and Xin Gao. Sd2: spatially resolved transcriptomics deconvolution through integration of dropout and spatial information. *Bioinformatics*, 2022. 2
- [36] Haoyang Li, Juexiao Zhou, Zhongxiao Li, Siyuan Chen, Xingyu Liao, Bin Zhang, Ruochi Zhang, Yu Wang, Shiwei Sun, and Xin Gao. A comprehensive benchmarking with practical guidelines for cellular deconvolution of spatial transcriptomics. *Nature Communications*, 2023. 2
- [37] Honglin Li, Chenglu Zhu, Yunlong Zhang, Yuxuan Sun, Zhongyi Shui, Wenwei Kuang, Sunyi Zheng, and Lin Yang. Task-specific fine-tuning via variational information bottleneck for weakly-supervised pathology whole slide image classification. In *CVPR*, 2023. 3
- [38] Yanghao Li, Haoqi Fan, Ronghang Hu, Christoph Feichtenhofer, and Kaiming He. Scaling language-image pre-training via masking. In *CVPR*, 2023. 3
- [39] Tiancheng Lin, Zhimiao Yu, Hongyu Hu, Yi Xu, and Chang-Wen Chen. Interventional bag multi-instance learning on whole-slide pathological images. In *CVPR*, 2023. 3
- [40] Kangning Liu, Weicheng Zhu, Yiqiu Shen, Sheng Liu, Narges Razavian, Krzysztof J Geras, and Carlos Fernandez-Granda. Multiple instance learning via iterative self-paced supervised contrastive learning. In *CVPR*, 2023. 3
- [41] Ming Y Lu, Tiffany Y Chen, Drew FK Williamson, Melissa Zhao, Maha Shady, Jana Lipkova, and Faisal Mahmood. Ai-based pathology predicts origins for cancers of unknown primary. *Nature*, 2021. 3
- [42] Ming Y Lu, Drew FK Williamson, Tiffany Y Chen, Richard J Chen, Matteo Barbieri, and Faisal Mahmood. Data-efficient and weakly supervised computational pathology on whole-slide images. *Nature biomedical engineering*, 2021. 1, 6
- [43] Ming Y Lu, Bowen Chen, Andrew Zhang, Drew FK Williamson, Richard J Chen, Tong Ding, Long Phi Le, Yung-Sung Chuang, and Faisal Mahmood. Visual language pre-trained multiple instance zero-shot transfer for histopathology images. In *CVPR*, 2023. 3
- [44] Ming Y Lu, Bowen Chen, Drew FK Williamson, Richard J Chen, Ivy Liang, Tong Ding, Guillaume Jaume, Igor Odintsov, Long Phi Le, Georg Gerber, et al. A visual-language foundation model for computational pathology. *Nature Medicine*, 2024. 3
- [45] Vivien Marx. Method of the year: spatially resolved transcriptomics. *Nature methods*, 2021. 1
- [46] Wenwen Min, Zhiceng Shi, Jun Zhang, Jun Wan, and Changmiao Wang. Multimodal contrastive learning for spatial gene expression prediction using histology images. *arXiv*, 2024. 2, 3
- [47] Reza Mirzazadeh, Zaneta Andrusivova, Ludvig Larsson, Phillip T Newton, Leire Alonso Galicia, Xesús M Abalo, Mahtab Avijgan, Linda Kvastad, Alexandre Denadai-Souza, Nathalie Stakenborg, et al. Spatially resolved transcriptomic profiling of degraded and challenging fresh frozen samples. *Nature Communications*, 2023. 6, 13
- [48] Jeffrey R Moffitt, Dhananjay Bambah-Mukku, Stephen W Eichhorn, Eric Vaughn, Karthik Shekhar, Julio D Perez, Nimrod D Rubinstein, Junjie Hao, Aviv Regev, Catherine Dulac, et al. Molecular, spatial, and functional single-cell profiling of the hypothalamic preoptic region. *Science*, 2018. 1
- [49] Ali Mortazavi, Brian A Williams, Kenneth McCue, Lorian Schaeffer, and Barbara Wold. Mapping and quantifying mammalian transcriptomes by rna-seq. *Nature methods*, 2008. 1
- [50] Muhammad Khalid Khan Niazi, Anil V Parwani, and Metin N Gurcan. Digital pathology and artificial intelligence. *The lancet oncology*, 2019. 3
- [51] Aaron van den Oord, Yazhe Li, and Oriol Vinyals. Representation learning with contrastive predictive coding. *arXiv preprint arXiv:1807.03748*, 2018. 4
- [52] Maxime Oquab, Timothée Darcet, Théo Moutakanni, Huy Vo, Marc Szafraniec, Vasil Khalidov, Pierre Fernandez, Daniel Haziza, Francisco Massa, Alaaeldin El-Nouby, et al. Dinov2: Learning robust visual features without supervision. *arXiv preprint arXiv:2304.07193*, 2023. 5, 14

- [53] Linhao Qu, Manning Wang, Zhijian Song, et al. Bi-directional weakly supervised knowledge distillation for whole slide image classification. In *NeurIPS*, 2022. 3
- [54] Linhao Qu, Zhiwei Yang, Minghong Duan, Yingfan Ma, Shuo Wang, Manning Wang, and Zhijian Song. Boosting whole slide image classification from the perspectives of distribution, correlation and magnification. In *CVPR*, 2023. 3
- [55] Alec Radford, Jong Wook Kim, Chris Hallacy, Aditya Ramesh, Gabriel Goh, Sandhini Agarwal, Girish Sastry, Amanda Askell, Pamela Mishkin, Jack Clark, et al. Learning transferable visual models from natural language supervision. In *ICML*, 2021. 2, 3
- [56] Anjali Rao, Dalia Barkley, Gustavo S França, and Itai Yanai. Exploring tissue architecture using spatial transcriptomics. *Nature*, 2021. 1
- [57] Andrew Rosenberg and Julia Hirschberg. V-measure: A conditional entropy-based external cluster evaluation measure. In *EMNLP-CoNLL*, 2007. 2
- [58] Antoine-Emmanuel Saliba, Alexander J Westermann, Stanislaw A Gorski, and Jörg Vogel. Single-cell rna-seq: advances and future challenges. *Nucleic acids research*, 2014. 1
- [59] Zhuchen Shao, Hao Bian, Yang Chen, Yifeng Wang, Jian Zhang, Xiangyang Ji, et al. Transmil: Transformer based correlated multiple instance learning for whole slide image classification. In *NeurIPS*, 2021. 3
- [60] Andrew H Song, Richard J Chen, Guillaume Jaume, Anurag J Vaidya, Alexander S Baras, and Faisal Mahmood. Multimodal prototyping for cancer survival prediction. In *ICML*, 2024. 3
- [61] Patrik L Ståhl, Fredrik Salmén, Sanja Vickovic, Anna Lundmark, José Fernández Navarro, Jens Magnusson, Stefania Giacomello, Michaela Asp, Jakob O Westholm, Mikael Huss, et al. Visualization and analysis of gene expression in tissue sections by spatial transcriptomics. *Science*, 2016. 1
- [62] Valentine Svensson, Roser Vento-Tormo, and Sarah A Teichmann. Exponential scaling of single-cell rna-seq in the past decade. *Nature protocols*, 2018. 1
- [63] Fuchou Tang, Catalin Barbacioru, Yangzhou Wang, Ellen Nordman, Clarence Lee, Nanlan Xu, Xiaohui Wang, John Bodeau, Brian B Tuch, Asim Siddiqui, et al. mrna-seq whole-transcriptome analysis of a single cell. *Nature methods*, 2009. 1
- [64] Wenhao Tang, Sheng Huang, Xiaoxian Zhang, Fengtao Zhou, Yi Zhang, and Bo Liu. Multiple instance learning framework with masked hard instance mining for whole slide image classification. In *CVPR*, 2023. 3
- [65] Wenhao Tang, Fengtao Zhou, Sheng Huang, Xiang Zhu, Yi Zhang, and Bo Liu. Feature re-embedding: Towards foundation model-level performance in computational pathology. In *CVPR*, 2024. 3
- [66] Laurens Van der Maaten and Geoffrey Hinton. Visualizing data using t-sne. *JMLR*, 2008. 2, 3
- [67] Eva Gracia Villacampa, Ludvig Larsson, Reza Mirzazadeh, Linda Kvastad, Alma Andersson, Annelie Mollbrink, Georgia Kokaraki, Vanessa Monteil, Niklas Schultz, Karin Sofia Appelberg, et al. Genome-wide spatial expression profiling in formalin-fixed tissues. *Cell Genomics*, 2021. 6
- [68] Eugene Vorontsov, Alican Bozkurt, Adam Casson, George Shaikovski, Michal Zelechowski, Kristen Severson, Eric Zimmermann, James Hall, Neil Tenenholtz, Nicolo Fusi, et al. A foundation model for clinical-grade computational pathology and rare cancers detection. *Nature medicine*, 2024. 2, 3
- [69] Haonan Wang, Peng Cao, Jiaqi Wang, and Osmar R Zaiane. Uctransnet: rethinking the skip connections in u-net from a channel-wise perspective with transformer. In *AAAI*, 2022. 1
- [70] Xiyue Wang, Sen Yang, Jun Zhang, Minghui Wang, Jing Zhang, Junzhou Huang, Wei Yang, and Xiao Han. Transpath: Transformer-based self-supervised learning for histopathological image classification. In *MICCAI*, 2021. 2, 3, 7, 14
- [71] Xiyue Wang, Junhan Zhao, Eliana Marostica, Wei Yuan, Jietian Jin, Jiayu Zhang, Ruijiang Li, Hongping Tang, Kanran Wang, Yu Li, et al. A pathology foundation model for cancer diagnosis and prognosis prediction. *Nature*, 2024. 2, 3
- [72] Zhong Wang, Mark Gerstein, and Michael Snyder. Rna-seq: a revolutionary tool for transcriptomics. *Nature reviews genetics*, 2009. 1
- [73] Ronald Xie, Kuan Pang, Sai Chung, Catia Perciani, Sonya MacParland, Bo Wang, and Gary Bader. Spatially resolved gene expression prediction from histology images via bimodal contrastive learning. In *NeurIPS*, 2023. 2, 3, 6, 7, 14
- [74] Hanwen Xu, Naoto Usuyama, Jaspreet Bagga, Sheng Zhang, Rajesh Rao, Tristan Naumann, Cliff Wong, Zelalem Gero, Javier González, Yu Gu, et al. A whole-slide foundation model for digital pathology from real-world data. *Nature*, 2024. 2, 3
- [75] Meilong Xu, Xiaoling Hu, Saumya Gupta, Shahira Abousamra, and Chao Chen. Semi-supervised segmentation of histopathology images with noise-aware topological consistency. In *ECCV*, 2025. 1
- [76] Yingxue Xu and Hao Chen. Multimodal optimal transport-based co-attention transformer with global structure consistency for survival prediction. In *ICCV*, 2023. 3, 6, 14
- [77] Hongrun Zhang, Yanda Meng, Yitian Zhao, Yihong Qiao, Xiaoyun Yang, Sarah E Coupland, and Yalin Zheng. Dtfmil: Double-tier feature distillation multiple instance learning for histopathology whole slide image classification. In *CVPR*, 2022. 3
- [78] Yunlong Zhang, Honglin Li, Yuxuan Sun, Sunyi Zheng, Chenglu Zhu, and Lin Yang. Attention-challenging multiple instance learning for whole slide image classification. In *ECCV*, 2024. 3
- [79] Yilan Zhang, Yingxue Xu, Jianqi Chen, Fengying Xie, and Hao Chen. Prototypical information bottlenecks and disentangling for multimodal cancer survival prediction. In *ICLR*, 2024. 3
- [80] Yiming Zhang, Zhuokai Zhao, Zhaorun Chen, Zhili Feng, Zenghui Ding, and Yining Sun. Rankclip: Ranking-consistent language-image pretraining. *arXiv*, 2024. 3
- [81] Fengtao Zhou and Hao Chen. Cross-modal translation and alignment for survival analysis. In *ICCV*, 2023. 3, 6, 14

- [82] Wenhui Zhu, Xiwen Chen, Peijie Qiu, Aristeidis Sotiras, Abolfazl Razi, and Yalin Wang. Dgr-mil: Exploring diverse global representation in multiple instance learning for whole slide image classification. In *ECCV*, 2024. [3](#)



# RankByGene: Gene-Guided Histopathology Representation Learning Through Cross-Modal Ranking Consistency

— Supplementary Material —

In the supplementary material, we begin with selection of the gene list in Section 6, followed by the data preprocessing in Section 7. Next, we provide implementation details in Section 8, followed by the reference of our baselines in Section 9. In Section 10, we describe the evaluation metrics in detail. More qualitative results are given in Section 11. To further demonstrate the effectiveness of our proposed method, the ablation study on different gene list is provided in Section 12. Finally, we discuss the limitation of our method in Section 13.

## 6. Selection of Gene List

Unlike existing methods that select highly expressed genes for gene-image alignment, we select prognosis-related genes from the Human Protein Atlas [4]. This resource provides gene lists corresponding to 31 different cancer types, each curated with validated genes most relevant to the specific cancer type. From these, we choose genes associated with the breast invasive carcinoma proteome to use with Breast ST data, and genes associated with the lung adenocarcinoma proteome to use with Lung ST data. These gene lists include both favorable and unfavorable genes and formed our initial gene lists. Since not all genes in our initial list are present in the ST data used for training and testing, we perform an intersection between the initial gene list and the genes available in the ST data to obtain the final gene lists. The final breast cancer gene list consists of 447 genes, while the lung cancer gene list includes 1,916 genes. Here, we show the top 20 genes with the highest expression values from each list separately. The complete gene lists will be made available upon the acceptance of our paper.

**Breast Gene List.** IGKC, TMSB10, ERBB2, IGHG3, IGLC2, IGHA1, GAPDH, ACTB, IGLC3, IGHM, SERF2, PSMB3, PFN1, ACTG1, KRT19, RACK1, MUCL1, CISD3, APOE, and MIEN1.

**Lung Gene List.** SFTPC, SFTPB, FTL, SCGB1A1, ITM2B, HLA-E, CD74, S100A6, UBC, SLPI, AGER, EEF2, IGHA1, MT2A, IFITM3, ACTB, IGKC, B2M, ID1, and TMSB4X.

## 7. Data Preprocessing

**Data Preprocessing for ST Datasets.** For all ST data used in this work, we utilize the standardized ST data collected from the HEST-1k [30] dataset. The associated WSIs are cut into patches of size  $224 \times 224$  at 20x magnification around each spot. To reduce experimental noise in raw

gene expression values, we adopt the smoothing method described in [17] by averaging each spot’s expression with its 8 neighboring spots before extracting gene features.

**Data Preprocessing for Survival Datasets.** For all WSIs used in the survival analysis task, we follow the data preprocessing pipeline described in DSMIL [34]. That is, to cut each WSI into patches of size  $224 \times 224$  at 20x magnification, with an intensity threshold of 20 used to filter out background patches.

## 8. Implementation Details

**Setting for Training Stage.** We use UNI [15] as the backbone for the image encoder, along with a 3-layer MLP projection head, and both the teacher and student image encoders share the same structure and initialization parameters. For the gene encoder, we use a 3-layer MLP with the same structure to transform raw gene expression values into gene features. Both image and gene features are in 1024 dimensions. We set the learning rate to 0.0001 for the image encoder and 0.001 for the gene encoder. The lower learning rate for the image encoder is because the architecture of the image encoder is more complex than the gene encoder. During training, ranking accuracy is calculated at each epoch using the gene embeddings instead of the raw gene expression values, and it serves as the criterion for model convergence. We set the number of training epochs to 100. The batch size is 64. We use the Adam optimizer with the EMA momentum rate set to 0.96 and the temperature for the gene-image contrastive loss set to 0.1. Finally, the backbone of the image encoder is used for feature extraction in downstream tasks. All experiments were conducted on an Nvidia Quadro RTX 8000 GPU with 48 GB of memory.

**Setting for Testing Stage: Gene Expression Prediction.** We use a 3-layer MLP as the gene prediction model, where the input is the gene-informed image feature, and the output is the predicted gene expression values. The ST data used in the training stage is split into training and validation sets at a ratio of 4:1. We select the best model on the validation set and evaluate it on the test set. For the model trained on breast ST data [7], we evaluate it on Breast-ST1 and Breast-ST2 datasets. For the model trained on lung ST data [47], we evaluate it on the Lung-ST dataset. The learning rate is set to 0.0001, and the number of training epochs is set to 20.

**Setting for Testing Stage: Survival Analysis.** We follow the implementation pipeline of MCAT [13] on survival analysis task, using the SGD optimizer with a learning rate of

0.0002 and train for 20 epochs.

## 9. Baseline Reference

We compare our method against image encoders with various architectures and pretrained on different datasets. These include ResNet-50 [23] pretrained on natural images from ImageNet, CTransPath [70] pretrained on pathology images using the MoCo [24] framework, and UNI pretrained on pathology images using the DINO [52] framework. Additionally, we also include gene-informed image encoders from existing state-of-the-art gene-image alignment methods, including the InfoNCE-based alignment described in HEST [30] (referred to as HEST-FT) and the CLIP-based alignment developed in BLEEP [73].

## 10. Details of Evaluation Metric

### 10.1. Gene Expression Prediction

In this study, we assess the performance of gene expression prediction on a per-sample basis. Specifically, we evaluate each model using three metrics: Pearson Correlation Coefficient (PCC), Mean Squared Error (MSE), and Mean Absolute Error (MAE). These metrics are computed for each gene at each spot and then aggregated to provide an overall evaluation. Assume that an ST sample contains  $n$  spots, each with  $m$  genes.

**Pearson Correlation Coefficient (PCC):** For the  $j$ -th gene in the  $i$ -th spot, the PCC ( $PCC_{i,j}$ ) is calculated as:

$$PCC_{i,j} = \frac{(\hat{y}_{i,j} - \bar{\hat{y}}_{i,j})(y_{i,j} - \bar{y}_{i,j})}{\sqrt{(\hat{y}_{i,j} - \bar{\hat{y}}_{i,j})^2} \sqrt{(y_{i,j} - \bar{y}_{i,j})^2}} \quad (7)$$

where  $\hat{y}_{i,j}$  and  $y_{i,j}$  are the predicted and ground truth expression values of the  $j$ -th gene at the  $i$ -th spot, respectively. To aggregate the PCC across all  $n$  spots for a specific gene  $j$ , we calculate  $PCC_j$  as follows:

$$PCC_j = \frac{\sum_{i=1}^n (\hat{y}_{i,j} - \bar{\hat{y}}_{i,j})(y_{i,j} - \bar{y}_{i,j})}{\sqrt{\sum_{i=1}^n (\hat{y}_{i,j} - \bar{\hat{y}}_{i,j})^2} \sqrt{\sum_{i=1}^n (y_{i,j} - \bar{y}_{i,j})^2}} \quad (8)$$

Finally, we take the average of  $PCC_j$  to compute the overall PCC across  $m$  genes:

$$PCC = \frac{1}{m} \sum_{j=1}^m PCC_j \quad (9)$$

**Mean Absolute Error (MAE):** MAE measures the average absolute difference between the predicted and ground truth values and is calculated as:

$$MAE(Y, \hat{Y}) = \frac{1}{n \cdot m} \sum_{i=1}^n \sum_{j=1}^m |y_{i,j} - \hat{y}_{i,j}| \quad (10)$$

**Mean Squared Error (MSE):** MSE quantifies the average squared difference between the predicted and ground truth values, defined as:

$$MSE(Y, \hat{Y}) = \frac{1}{n \cdot m} \sum_{i=1}^n \sum_{j=1}^m (y_{i,j} - \hat{y}_{i,j})^2 \quad (11)$$

Since we perform gene-image alignment using a selected list of cancer-related genes, we only evaluate the genes included in this list. When there are multiple ST samples in the test set, we calculate PCC, MAE, and MSE for each sample using the above formulas. The final results are then obtained by averaging these metrics across all samples.

## 10.2. Survival Analysis

Following previous methods [13, 76, 81], we perform 5-fold cross-validation to evaluate the model on the survival analysis task, reporting the cross-validated concordance index (C-Index) and its standard deviation (std) as metrics.

## 11. Additional Qualitative Result

**Visualization for Genes in Breast ST Data.** As shown in Figure 6, we select TUBA1C, ESRP1, MAL2, and RAB2A to visualize gene expression predictions. In the visualization, we specially observe the top left corner have high gene expression but there is almost no expression in BLEEP and HEST-FT predictions. On the other hand, the bottom left corner has almost zero expression in the ground truth while HEST-FT shows some spots with high expression.

**Visualization for Genes in Lung ST Data.** Figure 7 illustrates the predicted gene expression for BUB3, FAM98B, NOP56, and SCL38A2. In this case, we observe BLEEP and HEST-FT have high gene expression predictions around the WSI boundary while the ground truth have much lower expression. Furthermore, in the first row (BUB3), BLEEP and HEST-FT show very low expression in the bottom right corner which has the highest expression in the ground truth. On the other hand, our method can better capture the pattern in the ground truth.

**More t-SNE Visualization Results.** To further demonstrate the robustness and generalizability of our method, we present additional t-SNE visualizations using various samples from the breast ST dataset [7], as shown in Figure 8. Our method, incorporating both ranking loss and distillation, achieves superior performance, ensuring the highest separability across all tested samples. This consistency across diverse samples underscores the effectiveness of our approach in capturing the underlying distribution of gene expression values and mapping them to distinguishable image feature representations.



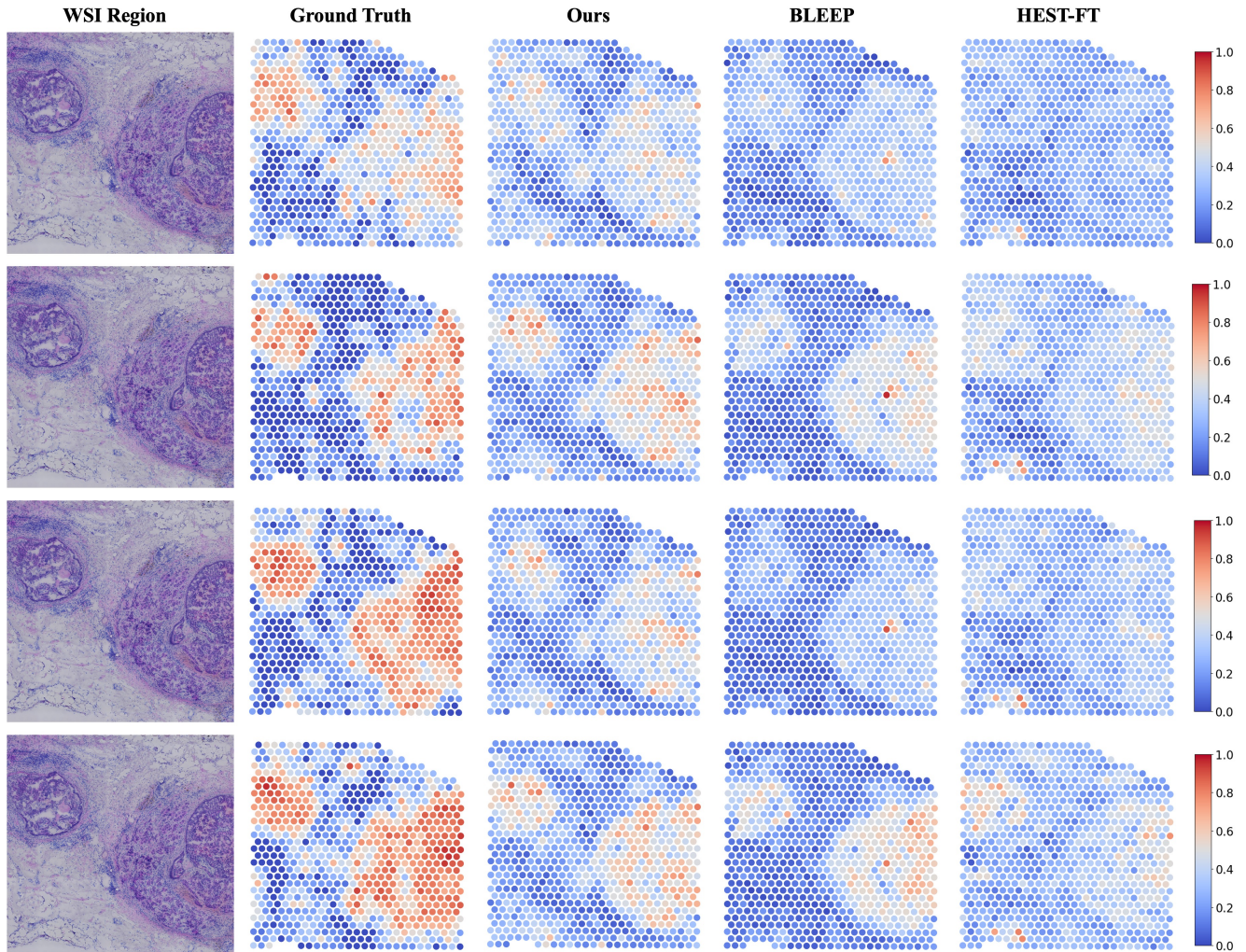


Figure 6. Additional visualizations of gene expression predictions for different genes using various methods, with all values normalized to the range of 0 to 1. From the first row to the fourth row: TUBA1C, ESRP1, MAL2, and RAB2A. Compared to the baseline, our predictions show the closest alignment with the ground truth.

## 12. Ablation Study

To evaluate the effectiveness of our selected gene list for downstream tasks, we perform an ablation study using different gene lists. Specifically, we use the top 250 highly expressed genes during training and evaluated the resulting image encoder on the survival analysis task. The results in Table 3 demonstrate that, compared to the highly expressed genes, our specifically chosen survival gene list improves the performance in survival analysis task by aligning image features with cancer-specific gene expression values.

## 13. Limitation

Our method has been validated only on breast and lung ST datasets, and further experiments on other organs, such as the brain, skin, kidney, and heart, are necessary to demon-

Image Encoder	C-Index	
	TCGA-BRCA	TCGA-LUAD
<i>RankByGene</i> w Top Expressed Genes	0.6762 ± 0.0383	0.5826 ± 0.0352
<i>RankByGene</i> w Cancer-Specific Genes	<b>0.6814 ± 0.0512</b>	<b>0.5945 ± 0.0293</b>

Table 3. Results for survival analysis on TCGA-BRCA and TCGA-LUAD datasets using different gene lists. The slide-level prediction is performed using the ABMIL [28] framework.

strate its generalizability. Additionally, due to resource limitations, we used UNI as the initialization for the image encoder, and further validation on other foundation models is required to confirm the effectiveness of our approach. Moreover, with the availability of higher-quality ST data (e.g., VisiumHD) [12], our method could be evaluated under higher-resolution settings to achieve more detailed gene-image alignment.

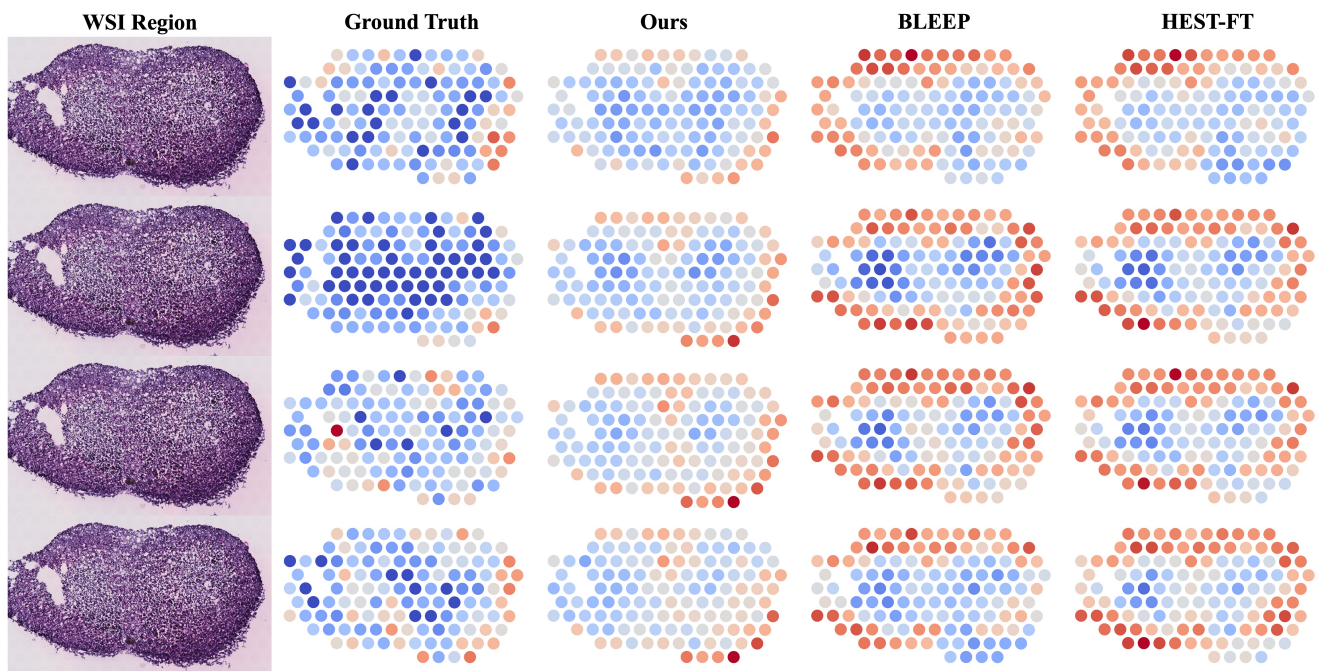


Figure 7. Additional visualizations of gene expression predictions for different genes using various methods, with all values normalized to the range of 0 to 1. From the first row to the fourth row: BUB3, FAM98B, NOP56, and SCL38A2. Compared to the baseline, our predictions show the closest alignment with the ground truth.



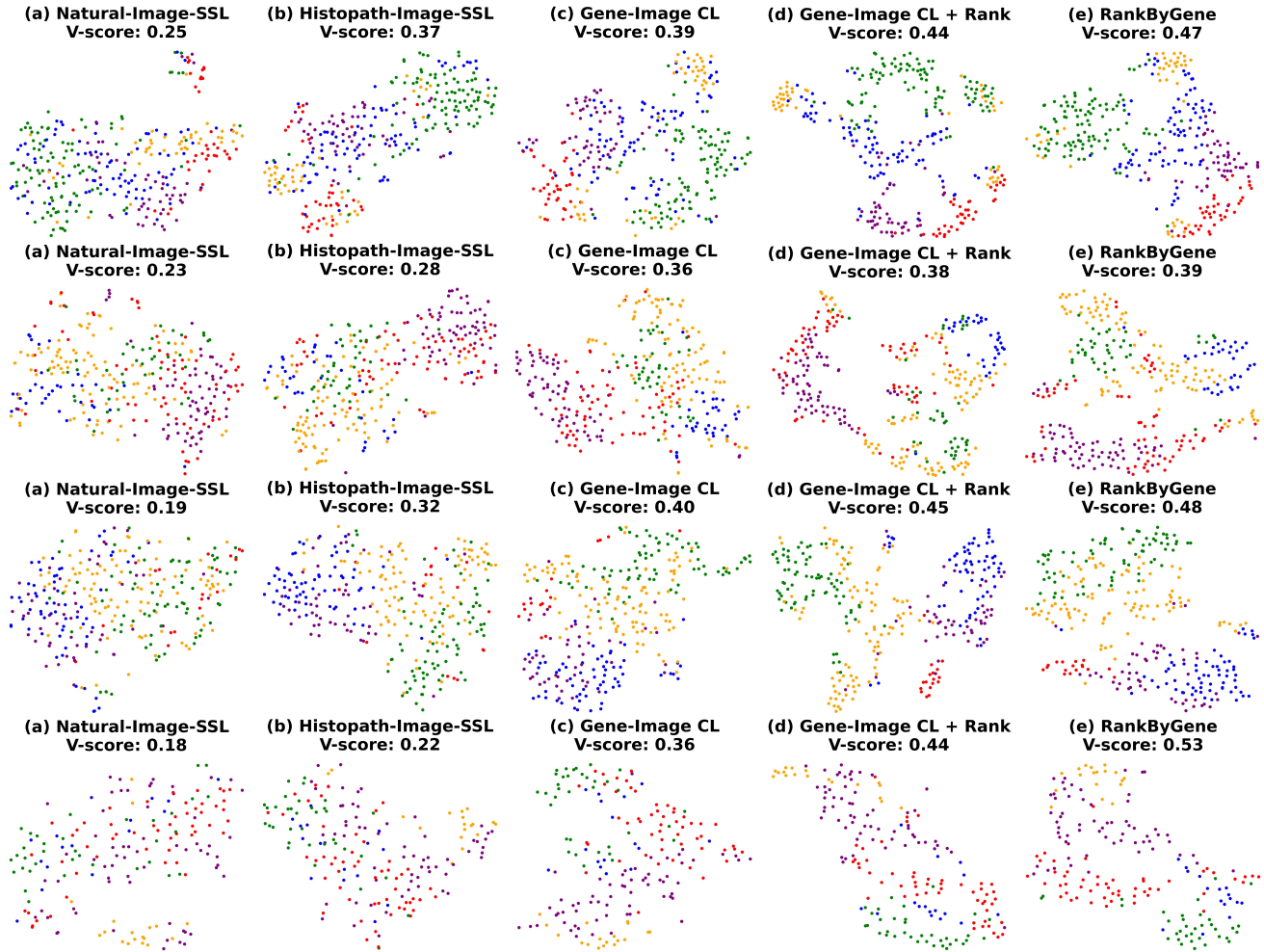


Figure 8. Additional t-SNE visualizations of different samples from the breast ST dataset [7]. From the first row to the fourth row: SPA131, SPA132, SPA134, and SPA139. Each visualization demonstrates the effectiveness of our method in achieving clear separability of clusters, highlighting the distinct spatial patterns of gene expression values across different samples. The consistent cluster formation across rows further emphasizes the robustness of our ranking loss and distillation approach in mapping gene expression data to image feature representations.